DOI: 10.13009/EUCASS2025-527
11TH EUROPEAN CONFERENCE FOR AERONAUTICS AND SPACE SCIENCES (EUCASS)

Gain-Scheduled LQR for RLV during In-Air Capturing: Trajectory Tracking, Recovery Limits and Replanning Criteria

Sunayna Singh⋆† *and Marco Sagliano*⋆
⋆*DLR, Institute of Space Systems*
Robert-Hooke-Strasse 7, 28359, Bremen, Germany
sunayna.singh@dlr.de · marco.sagliano@dlr.de
†Corresponding author

Abstract

'In-Air Capturing' is a unique launcher recovery approach in which a winged stage is retrieved mid-air by a towing aircraft, eliminating landing fuel requirements and increasing payload capacity. The method requires precise maneuvering of the reusable launch vehicle (RLV) relative to the aircraft to enable successful connection by a tethered capturing device despite external disturbances. This paper presents a guidance and control framework using a gain-scheduled Linear Quadratic Regulator (LQR) that adapts to the RLV's energy state for optimal performance. The controller guides the RLV into a wake-free 'mating zone' behind the aircraft for safe docking. Performance is evaluated under nominal conditions, disturbances, and initial state offsets. Capture feasibility is assessed through a Monte Carlo campaign, and the number of viable capture attempts is estimated.

1. Introduction

Over the past decades, the rise of the commercial launch industry has renewed the interest in reusable launch systems. Reusable launch vehicles (RLVs) have become key to meeting growing launch demands while reducing costs. Most current RLVs recover the first stage via downrange landing (DRL) or return to launch site (RTLS).[1] These methods require extra propellant for vertical landing, which increases lift-off mass and reduces payload. Alternatives like flyback boosters (using turbofans) or winged systems (like the space shuttle) also require significant propulsion and are not suitable for low-altitude booster recovery.[2] Non-propulsive recovery methods include parachutes, ballutes, and mid-air retrieval by helicopter. These offer savings for small rockets but become infeasible for larger stages. A more scalable solution is the 'In-Air Capturing (IAC)' method - a concept first patented by DLR in 2003,[2] where a winged booster is caught mid-glide and towed back by an aircraft .

Previous studies have compared IAC with other RLV recovery modes, highlighting its potential for significant mass and cost savings despite added structural complexity from wings and landing gear. A broader analysis of RLV concepts is performed by Dietlein et al,[3] covering performance, technical challenges, operational considerations, and system complexity. Cost trade-offs for different design configurations are evaluated by Wilken et al[4] using a top-down parametric model.

Figure 1 illustrates a generic mission profile, where a winged booster is recovered using IAC. The mission begins with vertical lift-off, followed by booster separation and atmospheric re-entry after main engine cut-off. The booster decelerates to a subsonic glide using aerodynamic braking. Meanwhile, a towing aircraft (TA) loiters at around 10 km altitude near the capture zone. IAC is executed when the RLV descends to between 8 km and 2 km altitude. To better understand the sequence of maneuvers involved, the IAC process is divided into five phases:[5]

1. *Formation Flight:* This phase begins when the RLV is sufficiently close to the TA, with a relative distance around 1 km. The TA descends from cruise altitude to enter a coordinated gliding formation with the RLV. It remains ahead while the RLV performs a rendezvous maneuver to align with the aircraft, while maintaining safe separation. Detailed subsystem modeling and analysis of this maneuver are provided by Singh et al.[6]
2. *Capture Phase:* During IAC, a capturing device attached to a tether is deployed from the TA (before the formation is achieved). The device, trailing behind the aircraft (as illustrated in Figure 1), holds position within a designated mating zone - a safe region for docking behind the TA. As the RLV enters this zone, the device autonomously navigates to the RLV and establishes a connection. This phase is similar to air-to-air refueling, where a hose

DOI: 10.13009/EUCASS2025-527

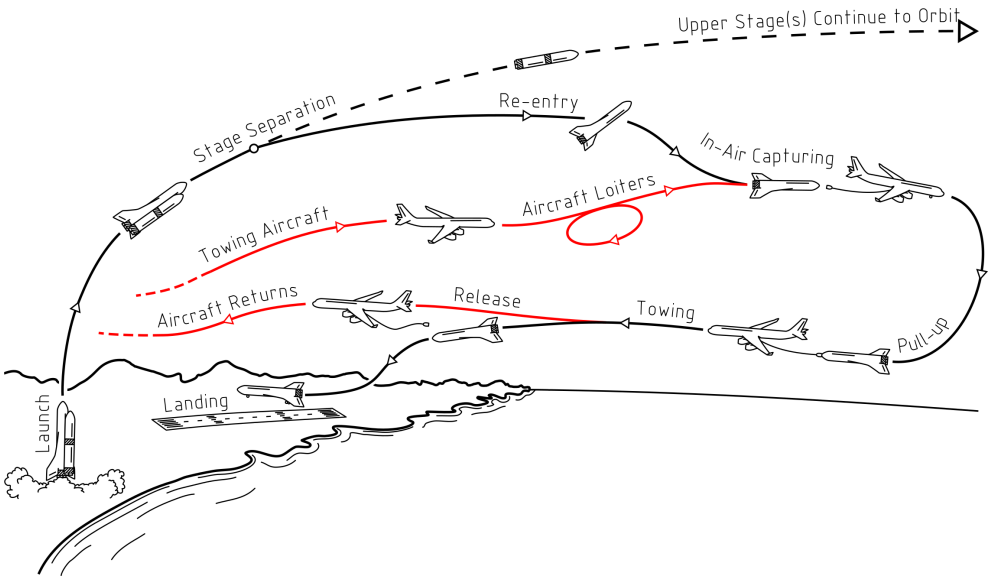

Figure 1: Schematic of the complete 'In-Air Capturing' mission cycle

connects the tanker aircraft to the receiving aircraft.[7] A detailed modeling of the capturing device and the tether dynamics is presented by Singh et al.[8–10] The formation flight and capture of the RLV must be completed between 8 km and 3 km altitude to allow margin for the pull-up maneuver.

3. *Pull-Up Maneuver:* After a successful connection, the TA increases engine thrust to initiate a coordinated pull-up maneuver. The combined system transitions from descent to climb, eventually reaching cruise altitude. From this point onward, the TA effectively functions as an external propulsion system for the unpowered RLV.[11] The pull-up maneuver must be attempted above an altitude of 2 km for safety.
4. *Tow-Back Phase:* The TA tows the RLV back to the launch site. While the TA provides the thrust to overcome aerodynamic drag, the RLV maintains level flight by generating sufficient lift to support its own weight.
5. *Release Maneuver:* As the system approaches the landing site, the RLV is released from the tow tether and performs an autonomous landing using its own landing gear.

Successful execution of the IAC maneuver relies on precise coordination between the RLV and the TA. This paper specifically examines the guidance and control strategies required by the RLV to attain formation flight and enable successful docking with the capturing device. To achieve this, a typical control strategy is employed, where a precomputed nominal path serves as guidance, and the controller is designed to correct any deviations from the expected state. However, this task is particularly challenging, as there is little to no existing literature on guidance and control for formation flight involving an unpowered RLV gliding with another vehicle. Furthermore, the IAC concept itself is novel. Therefore, this study aims to realistically model the system and rigorously assess the feasibility of the concept using standard yet advanced guidance and control approaches.

Prior to capture, the RLV must perform a controlled rendezvous and position itself at the mating zone. To ensure safety, the RLV's trajectory must maintain a safe separation from the TA. Extending the duration of formation flight is essential to allow multiple capture attempts, although this is challenging due to differing aerodynamic characteristics. Taking all these factors into account, an optimised rendezvous trajectory is generated for the RLV.[12] Assuming a fixed TA gliding trajectory in this study, the optimised RLV trajectory serves as guidance throughout the formation flight and capture phase. Since both vehicles are gliding during these phases, a robust control system is required to accurately follow the reference trajectory under varying flight conditions. To address this, a gain-scheduled Linear Quadratic Regulator (LQR), which adaptively tunes its gains based on the RLV's energy state is proposed. This enables the controller to handle deviations resulting from environmental disturbances, initial condition offsets, and system uncertainties.

The guidance and control system is evaluated for robust tracking in the presence of multiple external and environmental disturbances. Tracking performance is analysed separately for each disturbance to enhance understanding of system behavior and propose improvements that increase capture feasibility. A Monte Carlo campaign supports this assessment by exploring diverse initial states and disturbance scenarios. Error thresholds are analysed to identify when trajectory re-planning is required for successful capture. Additionally, a quantitative analysis of time spent within the mating zone provides insight into the number of feasible capture attempts within a given engagement window.

DOI: 10.13009/EUCASS2025-527

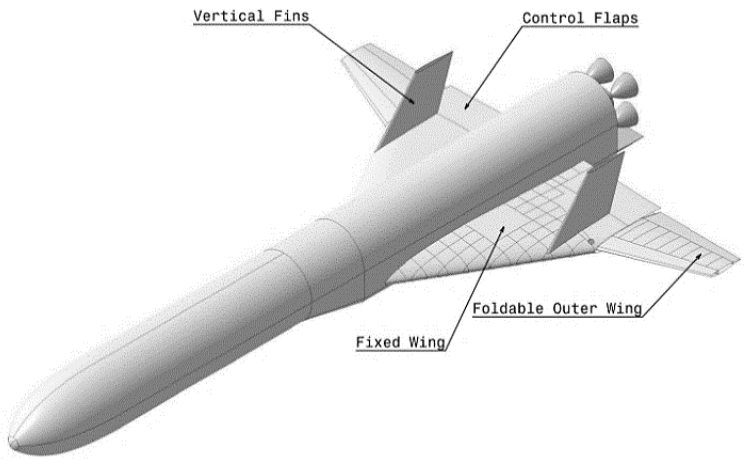

Figure 2: Reusable Launch Vehicle - RLVC4-IIIB[8]

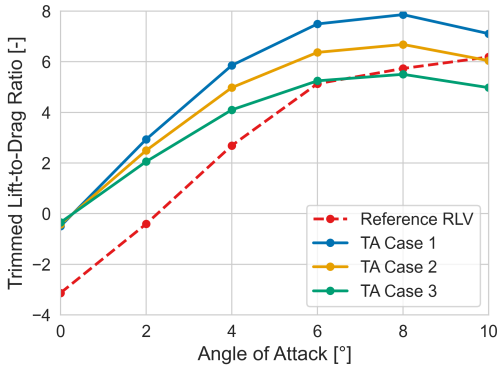

Figure 3: Aerodynamic performance of different RLV and TA configurations as a function of angle of attack

Hence, the structure of the paper is as follows. Section 2 describes the full-scale test cases and the modeling of the relevant subsystems. Section 3 presents the optimised RLV trajectory used for guidance, along with the proposed control methodology. The complete system architecture and the resulting closed-loop trajectory simulations are discussed in Section 4, including sensitivity analysis and a Monte Carlo campaign. Finally, Section 5 provides concluding remarks and discusses potential future developments.

2. Reference Vehicles and Dynamics

Although the complete IAC system involves three vehicles - the RLV, the TA, and the capturing device, only the RLV and TA are relevant to the current study. Section 2.1 provides a brief overview of these two full-scale vehicles and their aerodynamic characteristics, which play a critical role in ensuring successful capture. Since the TA trajectory is assumed to be fixed in this study, the focus is placed solely on the RLV dynamics. Section 2.2 introduces the fundamental equations of motion used for modeling the RLV. This is followed by the modeling of environmental and external disturbances, such as wake effects and wind, presented in Section 2.3.

2.1 Full-scale vehicles

During the IAC maneuver, the characteristics of the RLV primarily drive the design requirements for both the TA and the capturing device. Based on prior studies,[2,5,6,8] the RLV considered in this work is the first stage of a 3-stage-to-orbit launch system. This winged returning stage, designated RLVC4-IIIB (see Figure 2), features a unique swept-wing configuration.[13] During hypersonic re-entry, its outer wings remain folded to avoid shock-shock interactions. These wings are later deployed once the vehicle slows to subsonic speeds, as illustrated in Figure 2. This configuration enables a maximum lift-to-drag (L/D) ratio of up to 6 in the subsonic regime (see Figure 3), enabling it to glide longer and making it well-suited for IAC.[6] The RLV is expected to weigh approximately 80 tons during descent.

DOI: 10.13009/EUCASS2025-527

Capturing a large rocket stage requires a suitably sized TA. The retired Airbus A340-600 has been selected for this role due to its high thrust, substantial payload capacity, and cost-effective availability.[6,14] Powered by four Rolls-Royce Trent 556 engines and equipped with an advanced flight control system, the A340-600 meets the operational demands for IAC of the RLVC4-IIIB. To enable prolonged formation flight, aerodynamic compatibility between the TA and RLV is essential. While typical commercial aircraft have lift-to-drag (L/D) ratios up to 20, this gap is narrowed using drag-inducing surfaces such as spoilers and landing gear.[6]

Figure 3 compares the aerodynamic performance of three TA configurations with that of the reference RLV. TA Case 1, selected in previous studies, features deployed front and side landing gear and -20° spoiler deflection.[6] Both the RLV and TA Case 1 configurations were analysed using CFD,[15] with results shown in the figure. The analysis reveals a significant mismatch in aerodynamic performance between TA Case 1 and the RLV, making prolonged formation flight - and thus multiple capture attempts - challenging.[6,16] To better evaluate feasibility, two additional configurations were introduced:[12] TA Case 2, which increases base drag by 17.7%, and TA Case 3, which increases it by 35%. While Case 3 provides the closest aerodynamic match to the RLV, Case 2 is considered more realistic. Hence, TA Case 2 will be used to assess the limits of the IAC concept and define its operational boundaries.

2.2 Equations of motion

The RLV is modeled using standard point-mass dynamics for an unpowered vehicle over a rotating spherical Earth, assuming no wind and constant mass. The corresponding equations of motion are given as follows:[17]

$$\dot{r} = v \cdot \sin(\gamma) \tag{1}$$

$$\dot{\phi} = \frac{v \cdot \cos(\gamma) \cdot \cos(\psi)}{r \cdot \cos(\lambda)} \tag{2}$$

$$\dot{\lambda} = \frac{v \cdot \cos(\gamma) \cdot \sin(\psi)}{r} \tag{3}$$

$$\begin{aligned}\dot{v} = &-\frac{D}{m} - \frac{\mu}{r^2} \cdot g \cdot \sin(\gamma) \\ &+ \omega^2 \cdot r \cdot \cos(\lambda) \cdot (\sin(\gamma) \cdot \cos(\lambda) - \cos(\gamma) \cdot \sin(\psi) \cdot \sin(\lambda))\end{aligned} \tag{4}$$

$$\begin{aligned}\dot{\gamma} = &\frac{L \cdot \cos(\sigma)}{m \cdot v} + \frac{v}{r} \cdot \cos(\gamma) \\ &- \frac{\mu}{v \cdot r^2} \cdot g \cdot \cos(\gamma) + 2 \cdot \omega \cdot \cos(\psi) \cdot \cos(\phi) \\ &+ \frac{\omega^2 \cdot r}{v} \cdot \cos(\phi) \cdot (\cos(\gamma) \cdot \cos(\phi) + \sin(\gamma) \cdot \sin(\psi) \cdot \sin(\phi))\end{aligned} \tag{5}$$

$$\begin{aligned}\dot{\psi} = &\frac{L \cdot \sin(\sigma)}{m \cdot v \cdot \cos(\gamma)} - \frac{v}{r} \cdot \cos(\gamma) \cdot \cos(\psi) \cdot \tan(\phi) \\ &+ 2 \cdot \omega \cdot (\tan(\gamma) \cdot \sin(\psi) \cdot \cos(\phi) - \sin(\phi)) \\ &- \frac{\omega^2 \cdot r}{v \cdot \cos(\gamma)} \cdot \cos(\psi) \cdot \sin(\phi) \cdot \cos(\phi)\end{aligned} \tag{6}$$

Here, r is the radial distance from the center of the Earth to the vehicle, λ and ϕ denote the longitude and latitude, respectively, v is the Earth-centered velocity, γ is the flight path angle, and ψ is the heading angle of the relative velocity vector, measured clockwise from geographic north. The terms D and L represent the aerodynamic drag and lift forces, respectively, which are functions of the angle of attack and Mach number, and are defined as:

$$L = \frac{1}{2}\rho {v_{\text{air}}}^2 S C_L \tag{7}$$

$$D = \frac{1}{2}\rho {v_{\text{air}}}^2 S C_D \tag{8}$$

Here, ρ is the atmospheric density (varies with altitude), v_{air} is the air-relative speed of the vehicle, S is the reference area of the vehicle, C_L and C_D represent the lift and drag coefficients respectively.

In this study, the rate of change of angle of attack ($\dot{\alpha}$) and bank angle ($\dot{\sigma}$) are selected as the control variables, denoted by u_α and u_σ, respectively. This modeling choice enables smoother and more physically realistic trajectories

DOI: 10.13009/EUCASS2025-527

by avoiding abrupt changes in the angle of attack (α) and bank angle (σ). Incorporating these rates into the previously defined equations of motion results in a control-affine system, where the control inputs enter the dynamics linearly:

$$\dot{\alpha} = u_\alpha, \quad \dot{\sigma} = u_\sigma \tag{9}$$

The angular rates ($\dot{\alpha}$ and $\dot{\sigma}$) of the control inputs are limited by $\pm 3^\circ/\text{s}$. Thus, the state vector becomes:

$$\mathbf{x} = [r,\ \phi,\ \lambda,\ v,\ \gamma,\ \psi,\ \alpha,\ \sigma]^T \tag{10}$$

2.3 Environmental and external disturbances

For this study, the main atmospheric and environmental perturbations - namely wind, wake, and atmospheric density - have been addressed. These disturbances directly affect aerodynamic forces, guidance accuracy, and control robustness, making their inclusion essential for a realistic assessment of system performance.

Wind

Wind is a significant source of uncertainty for unpowered vehicles, especially during precision maneuvers such as those required in IAC. Its characteristics vary with altitude, season, and geographic location, making it an extremely variable disturbance. To evaluate the guidance and control system under realistic conditions, this study employs the Horizontal Wind Model 2007 (HWM07), available as a MATLAB-Simulink package. HWM07 is an empirical model that balances physical fidelity and computational efficiency, capturing atmospheric wind behavior based on decades of measurement data.[18] Figure 4 shows example wind profiles generated along the reference trajectory from Section 4.1, evaluated at different days and times. It can be observed that the meridional (north-south) winds tend to be smaller in magnitude and variation compared to the zonal (east-west) winds. For simplicity, a single wind profile is used throughout the study; this reference case is shown with dotted lines in the figure.

As aerodynamic coefficients depend on airspeed, wind directly affects vehicle dynamics. The ground velocity (v) is first transformed into North-East-Down (NED) components,[19]

$$v_n = -v\cos(\gamma)\cos(\psi) \tag{11}$$
$$v_e = \ \ v\cos(\gamma)\sin(\psi) \tag{12}$$
$$v_d = \ \ v\sin(\gamma) \tag{13}$$

Then, the wind vector (also expressed in the NED frame) is subtracted to obtain the air-relative velocity.

$$\mathbf{v}_{\text{air}} = \mathbf{v}_{\text{NED}} - \mathbf{w}_{\text{NED}} \tag{14}$$

where, $\mathbf{w}_{\text{NED}} = \begin{bmatrix} -w_m,\ w_z,\ 0 \end{bmatrix}^T$ and $\mathbf{v}_{\text{NED}} = \begin{bmatrix} v_n,\ v_e,\ v_d \end{bmatrix}^T$. Here, w_m and w_z represent the meridional and zonal components of wind respectively.

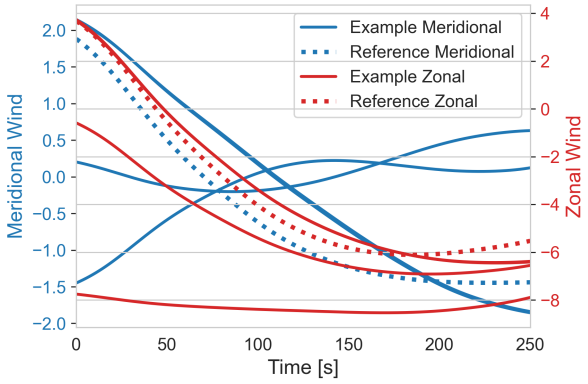

Figure 4: Horizontal Wind Model 07 profiles - meridional and zonal components

DOI: 10.13009/EUCASS2025-527

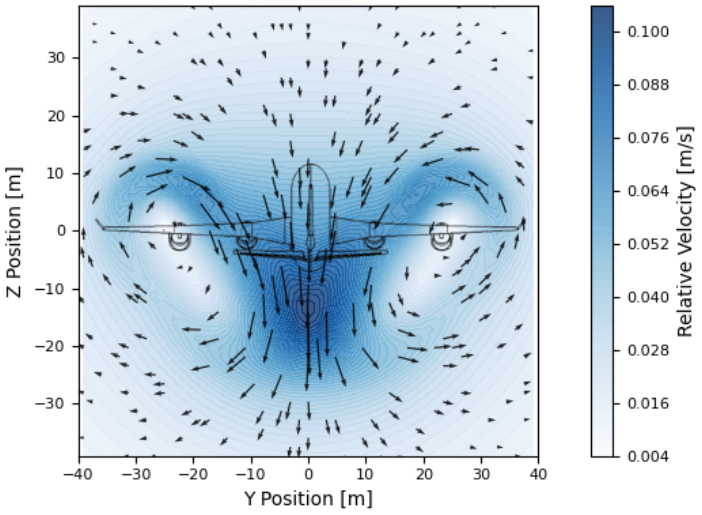

Figure 5: Relative wake velocity contours 250 m behind the aircraft at 10° angle of attack

Wake

Previous CFD (RANS) studies[6,15] of the TA's wake behavior shows that significant aerodynamic disturbances can extend up to 350 m behind the aircraft's nose. Since the capture is expected to occur behind the TA, both the RLV and the capturing device are likely to be affected by the wake. Figure 5 shows the contour of the relative wake velocity, defined as the ratio of vertical to lateral velocity components (V_{wz}/V_{wy}), evaluated 250 m behind the aircraft center of gravity.[9] Prior studies indicate that while the RLV experiences temporary perturbations in angle of attack upon entering the wake, it can regain stability quickly.[6] In contrast, the smaller capturing device loses control entirely when exposed to the wake.[9] Therefore, to ensure successful docking, the capture maneuver must be performed outside the most turbulent regions of the wake, in an area called mating zone (explained further in Section 3.1). Nonetheless, to reach the mating zone, the RLV is expected to pass through the aircraft wake and encounter significant disturbances. Therefore, accurately modeling this disturbance is essential for evaluating the robustness of the RLV's guidance and control system.

Table 1: Simulation flight point for wake analysis

Parameter	**Value**
Velocity [m/s]	142.39
Mach [-]	0.45
Altitude [m]	6000
Pressure [Pa]	47248.92
Density [kg/m^3]	0.66065

From the studies performed by Kucukosman et al,[15] a comprehensive wake disturbance database was developed at a single flight point shown in Table 1. The wake behavior was evaluated at different angle of attacks ranging between 0° and 10°. In this study, key data such as the variation in air-relative velocity components ($\mathbf{\Delta V_{wake}} = [\Delta V_{wx}, \Delta V_{wy}, \Delta V_{wz}]^T$) and turbulent kinetic energy (k) were obtained. The wake module used in the simulation is based on look-up tables that provide changes in air-relative velocity as a function of the RLV's position relative to the towing aircraft. To model turbulence, time-dependent velocity fluctuations are superimposed on this data using:

$$\mathbf{\Delta v}_{\text{wake}} = \mathbf{\Delta V_{wake}} + \mathbf{v'_w} \tag{15}$$

where, $\mathbf{v'_w} = [v'_{wx}, v'_{wy}, v'_{wz}]^T$ represents random velocity fluctuations with the standard deviation v'_w. v'_w is the root mean square of the velocity fluctuations caused by turbulence and can be directly linked to turbulent kinetic energy (k) by:[20]

$$v'_w = \sqrt{\frac{1}{3}\left({v'_{wx}}^2 + {v'_{wyx}}^2 + {v'_{wz}}^2\right)} = \sqrt{\frac{2}{3}k} \tag{16}$$

DOI: 10.13009/EUCASS2025-527

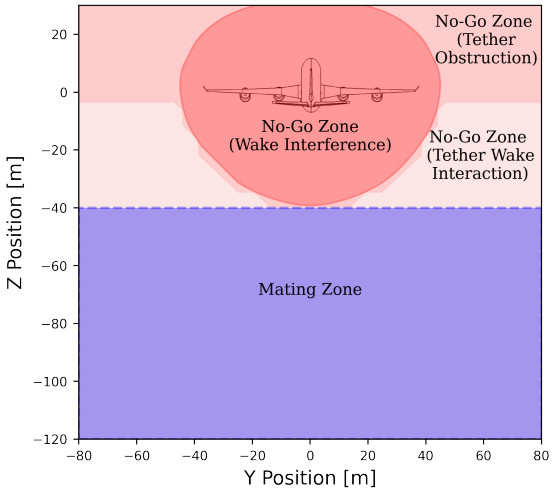

Figure 6: Mating zone for the docking maneuver between capturing device and RLV, 250 m behind the TA[12]

It should be noted that the CFD simulations were carried out using a steady-state solver (`rhoSimpleFoam`), which results in a simplified approximation of turbulence compared to the complex, unsteady flow structures typically observed in aircraft wake. Nonetheless, for the purposes of this study, the simplified model provides an adequate representation of the wake effects. Due to the unavailability of wake data at multiple flight conditions, the wake effect is assumed to remain constant throughout the trajectory. In reality, the intensity and structure of the wake would vary with factors such as air density, altitude, and flight speed.

The resulting velocity perturbation is then added to the nominal air-relative velocity, causing the RLV to experience a turbulent flow field. Thus, Equation 14 becomes:

$$\mathbf{v}_{\text{air}} = \mathbf{v}_{\text{NED}} - \mathbf{w}_{\text{NED}} + \Delta\mathbf{v}_{\text{wake}} \tag{17}$$

Atmospheric density

Since realistic atmospheric conditions vary significantly with altitude, temperature, time of day, and geographic location, relying on a single atmospheric model is insufficient to determine whether the guidance and control system remains robust under off-nominal conditions. To address this, a normally distributed random disturbance with a standard deviation of 7.5% is applied to the atmospheric density values derived from the standard US76 model. It impacts the lift and drag of the vehicle (Equations 7 and 8) directly, even if speed and angle of attack stay the same. This allows the simulation to better reflect the variability encountered in real-world scenarios and supports a more comprehensive feasibility analysis.

3. Guidance and Control

This section outlines the guidance and control strategy developed for the RLV during IAC. Section 3.1 presents the optimised rendezvous trajectory, which serves as the guidance reference until the RLV is captured. The optimisation framework, including the underlying logic, assumptions, and tools used, is also described. Section 3.2 details the design and implementation of the gain-scheduled Linear Quadratic Regulator (LQR) used to track the reference trajectory.

3.1 Nominal guidance trajectory

As shown earlier in Figure 3, the aerodynamic performance of the TA and RLV are similar but not perfectly matched for the reference full-scale configurations. Even in TA Case 2 (reference for current study), the TA exhibits a slightly higher L/D ratio than the RLV. As a result, during formation flight, the RLV cannot sustain a perfectly parallel path at constant velocity and separation. Instead, it gradually descends relative to the TA. Although the rendezvous maneuver for the formation flight begins at a relative distance of approximately 1 km from the TA, a specific criterion is established to define successful formation. This ensures that the necessary conditions for initiating the capture phase are met.

During the capture phase, the RLV must enter a predefined mating zone to enable successful docking. This zone is defined based on the maneuverability limits of the capturing device and the need to avoid intense wake disturbances.[12]

DOI: 10.13009/EUCASS2025-527

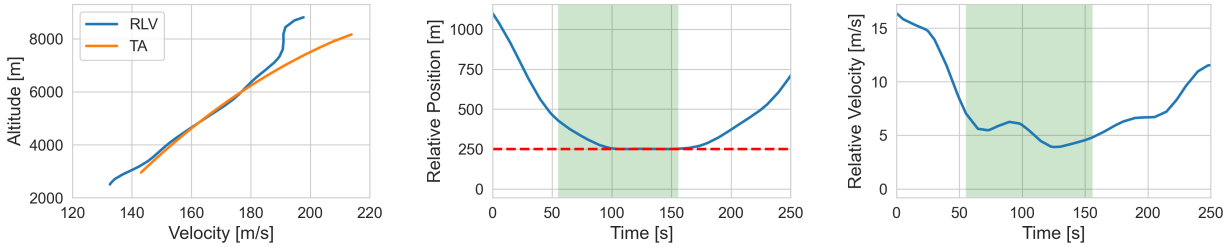

Figure 7: Rendezvous trajectory simulation of the RLV with TA Case 2[12]

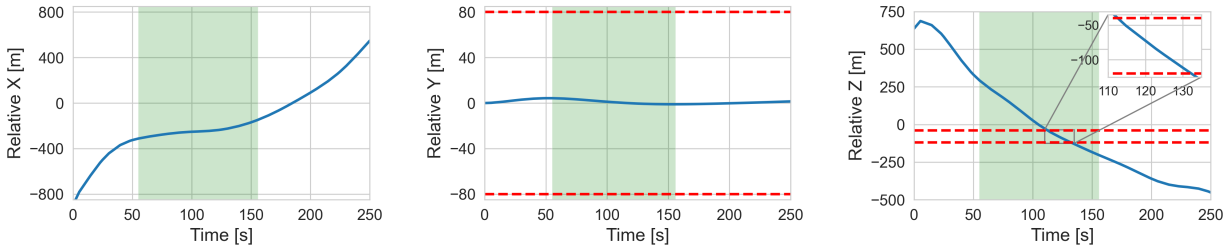

Figure 8: Position of RLV relative to TA Case 2 with mating zone (red-dash)[12]

As shown in Figure 6, the mating zone is nominally located 250 m behind the TA's center of gravity and spans 80 m by 160 m in the vertical and lateral directions. However, the actual longitudinal position of this zone depends on the length of the tether, which can vary between 150 m and 300 m using a winch mechanism. While the size of the box remains fixed, its location must be redefined according to the tether length. The winch mechanism offers additional flexibility to correct for small mismatches in relative position during the final approach. To enable multiple capture attempts within a single engagement window, the time the RLV spends inside the mating zone should be maximized.

Based on the above requirements, the rendezvous trajectory is optimised using GPOPS-II,[21] a MATLAB-based software for solving general nonlinear optimal control problems, with the objectives and constraints summarised as follows:[12]

- Formation flight must occur within an altitude range of 3000 m to 8000 m.
- The RLV must approach the TA from behind and starting at a higher altitude.
- The formation criteria is met when the relative distance between the RLV and TA is 450 m or less, corresponding to the operational limit of the close-range navigation system.
- During formation, the RLV should reach a designated mating zone at a relative distance of 250 m from the TA.
- The relative velocity of the RLV with respect to the TA must be minimized to allow the RLV to remain within the mating zone for an extended duration.
- Control surfaces must remain unsaturated throughout the formation flight phase.

Since the RLV's position and velocity relative to the TA significantly influence the problem dynamics, the initial starting point is included as part of the optimisation. To simplify the scenario, both the RLV and TA are assumed to fly eastward (90° azimuth from North).

Figure 7 shows the optimised rendezvous trajectory of the RLV with TA Case 2. The altitude-velocity profile indicates only partial overlap between the RLV and TA trajectories, mainly due to the difference in aerodynamic performance (see Figure 3). A closer look at the relative position and velocity of the RLV with respect to the TA, shown in Figure 7, indicates that formation flight highlighted by the green shaded region is maintained for approximately 100 s. The formation criteria is met at a relative distance of 450 m and continues until the RLV leaves the mating zone at 250 m relative distance from the aircraft.

Figure 8 shows the relative X, Y, and Z positions of the RLV with respect to the TA during the rendezvous. The bounds of the mating zone are indicated by red dashed lines in the lateral (Y) and vertical (Z) directions. It is observed that the RLV remains within this mating zone for about 20 s. A margin of 20 s could provide sufficient time for two docking attempts during the capture phase, assuming no major uncertainties or anomalies occur. This is supported by previous studies,[9,10] which show that the capturing device typically requires around 20 s to perform a 30 m maneuver. Additionally, Figure 9 shows the profiles of the angle of attack and bank angle, along with their rates of change, which

DOI: 10.13009/EUCASS2025-527

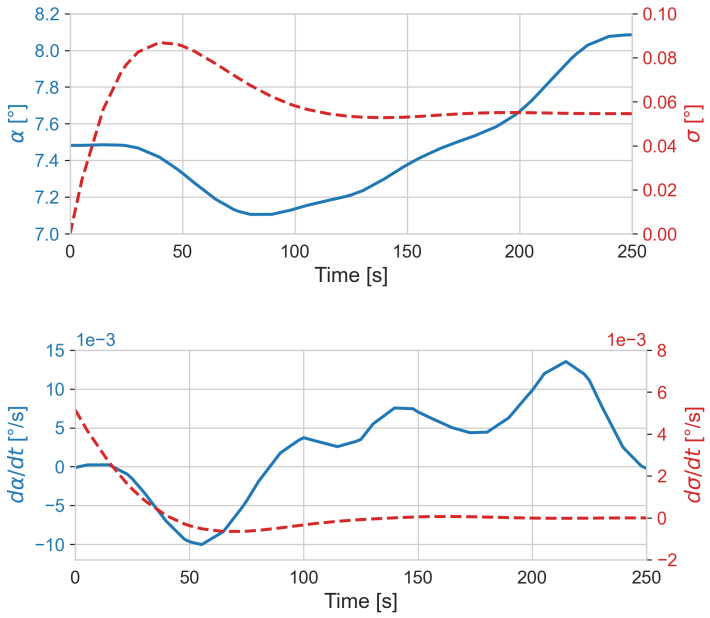

Figure 9: Angle of attack and bank angle (top) with corresponding control rates (bottom) for RLV rendezvous considering TA Case 2[12]

served as control inputs in the optimisation process. It can be observed that the control rates remain well within the imposed limits of ±3°/s, and no significant sharp maneuvers are performed.

Hence, this trajectory is used as the guidance for the RLV in the nominal scenario. While the guidance does not account for environmental disturbances or uncertainties, its robustness against deviations and the need for corrective actions will be evaluated through a dedicated Monte Carlo campaign in this study.

3.2 Gain-scheduled LQR

During the formation flight and capture phase, the complete IAC system operates in an unpowered descending flight. The RLV must accurately track the nominal guidance trajectory despite the presence of errors, system uncertainties, and external disturbances in a dynamically changing environment. To achieve this, a robust and adaptive control architecture is employed, combining feedforward control with gain-scheduled Linear Quadratic Regulator (LQR) feedback. In other words, the total control input $\mathbf{u}(t)$ can be expressed as the sum of the feedforward and feedback components:

$$\mathbf{u}(t) = \mathbf{u_{ff}}(t) + \mathbf{u_{fb}}(t)$$

The process of controller design is explained as follows:

1. *Feedforward Control*: The nominal guidance trajectory is optimised to maximize the duration spent within the mating zone. As a result, it includes specific maneuvering actions that are critical to mission success. The corresponding control inputs required to execute these maneuvers are precomputed during the trajectory optimisation and directly applied as feedforward inputs. This approach ensures that the desired trajectory shape is preserved and eliminates steady-state tracking errors under ideal conditions. The expression for the feedforward control input can be directly obtained from the nominal trajectory and is given by Equation 9.

$$\mathbf{u_{ff}}(t) = [u_\alpha(t),\ u_\sigma(t)]^T \tag{18}$$

2. *Feedback Control*: A gain-scheduled LQR is employed to compensate for deviations from the nominal trajectory. This feedback mechanism addresses tracking errors that may arise due to off-nominal initial conditions, system uncertainties, or external disturbances. Since mechanical energy plays a critical role in the behavior of an unpowered RLV with limited aerodynamic control authority, gain scheduling is performed as a function of the system's total mechanical energy per unit mass, given by:

$$E = \frac{1}{2}v^2 + g_0 h \tag{19}$$

DOI: 10.13009/EUCASS2025-527

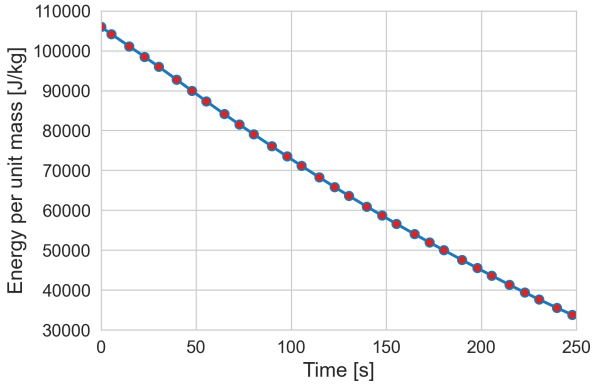

Figure 10: Specific energy of the RLV at different operating points along the reference trajectory

where E is the total mechanical energy per unit mass (specific mechanical energy), v is the speed of the vehicle, g_0 is the standard gravitational acceleration (typically 9.80665 m/s^2), and h is the altitude of the vehicle. This energy-based scheduling ensures that the feedback gains remain effective across different flight regimes, even under off-nominal conditions. The variation of mechanical energy with time at the selected operating points along the trajectory is shown in Figure 10.

To compute the LQR gains at each operating point, the nonlinear system is first linearized about that point using the small-perturbation finite-difference approach.[22] The corresponding state matrix $\mathbf{A}$ and the input matrix $\mathbf{B}$ at each operating point are computed as:

$$\mathbf{A}_{i,j} \approx \frac{f(\mathbf{x} + \delta x_j\, \mathbf{e}_j, \mathbf{u}) - f(\mathbf{x} - \delta x_j\, \mathbf{e}_j, \mathbf{u})}{2\delta x_j} \tag{20}$$

$$\mathbf{B}_{i,k} \approx \frac{f(\mathbf{x}, \mathbf{u} + \delta u_k\, \mathbf{e}_k) - f(\mathbf{x}, \mathbf{u} - \delta u_k\, \mathbf{e}_k)}{2\delta u_k} \tag{21}$$

where $f(\mathbf{x}, \mathbf{u})$ represents the nonlinear system dynamics, $\mathbf{e}_j$ and $\mathbf{e}_k$ are unit vectors in the directions of the j-th state and k-th input, respectively, and δx_j, δu_k are small perturbations applied to the state and input variables. For the current study, the system is perturbed using small finite differences: altitude by $\delta_{\text{rad}} = 10$ m, velocity by $\delta_{\text{vel}} = 1$ m/s, and angular quantities (e.g., flight path angle, azimuth, or angle of attack) by $\delta_{\text{angle}} = 10^{-6}$ rad.

At each operating point, the LQR gain matrix $\mathbf{K}_i$ is computed by solving the continuous-time Algebraic Riccati Equation.[23] The objective is to minimize the following cost function:

$$J = \int_0^\infty \left(\tilde{\mathbf{x}}^\top \mathbf{Q} \tilde{\mathbf{x}} + \tilde{\mathbf{u}}^\top \mathbf{R} \tilde{\mathbf{u}}\right) dt \tag{22}$$

where $\tilde{\mathbf{x}}$ is the deviation from the reference state, $\tilde{\mathbf{u}}$ is the deviation from the reference control, $\mathbf{Q} \geq 0$ is the state weighting matrix, and $\mathbf{R} > 0$ is the control weighting matrix given by:

$$\mathbf{R} = \text{diag}(2 \times 10^5,\, 2 \times 10^5), \quad \mathbf{Q} = \text{diag}(1.5 \times 10^{-5},\, 0.01,\, 0.075,\, 0.05,\, 10^4,\, 10^4,\, 10^6,\, 5000)$$

The optimal feedback gain $\mathbf{K}_i$ is obtained by first solving the Algebraic Riccati Equation:

$$\mathbf{A}_i^\top \mathbf{P}_i + \mathbf{P}_i \mathbf{A}_i - \mathbf{P}_i \mathbf{B}_i \mathbf{R}^{-1} \mathbf{B}_i^\top \mathbf{P}_i + \mathbf{Q} = 0 \tag{23}$$

where $\mathbf{P}_i$ is the unique positive semi-definite solution. The corresponding LQR gain is then given by:

$$\mathbf{K}_i = \mathbf{R}^{-1} \mathbf{B}_i^\top \mathbf{P}_i \tag{24}$$

This procedure is repeated for all $i = 1, \ldots, N$, resulting in a library of gain matrices $\mathbf{K}_i$, for distinct operating points along the trajectory. These are used in the gain-scheduled controller based on the current energy state of RLV. It is assumed that the full state vector is measurable and available for feedback. Hence, the expression of the feedback control becomes:

$$\mathbf{u_{fb}}(t) = -K\left(E(t)\right)\left(\mathbf{x}(t) - \mathbf{x}_{\text{ref}}(t)\right) \tag{25}$$

DOI: 10.13009/EUCASS2025-527

4. Closed-loop Simulations

The full system described in the previous section is illustrated in the closed-loop system architecture shown in the Figure 11. It includes the guidance module - an optimised trajectory ($\mathbf{x_{ref}}$) generated using GPOPS-II, and the feedforward control ($\mathbf{u_{ff}}$) derived from this trajectory. Additionally, it comprises an energy-based gain-scheduled LQR feedback controller ($\mathbf{u_{fb}}$) and the RLV dynamics, which account for external disturbances and uncertainties. The simulation is implemented in MATLAB using a fixed time step of 0.1 s. Numerical integration is performed using a fourth-order Runge-Kutta (RK4) integrator.

To better evaluate the controller's performance, both open-loop and closed-loop simulations are compared under scenarios with and without disturbances. This comparison demonstrates the extent to which the feedback controller mitigates the effects of external disturbances. It is assumed that the trajectory starts from the nominal initial condition with no errors in the initial state. A comprehensive Monte Carlo study will be presented in Section 4.2 to analyse the impact of initial state errors and to establish thresholds and boundaries for guidance replanning. Figure 12 presents trajectory simulations for RLV rendezvous across all four open and closed-loop scenarios. In the open-loop simulations, only the feedforward control inputs are applied. In the absence of disturbances, the open-loop and closed-loop trajectories are identical, as no feedback action is triggered without external disturbances or deviations from the initial state. The system simply follows the nominal trajectory. However, looking at the closed-loop and open-loop scenarios with disturbances, some major deviations can be observed.

In the presence of disturbances, significant deviations arise for both open-loop and closed-loop trajectories. The altitude-velocity profile notably diverges from the nominal case. When examining the relative position with respect to the TA, both scenarios fail to maintain the required relative distance of 250 m. In fact, they fall outside the 150-300 m range of the capturing device, and neither scenario successfully enters the mating zone. A closer inspection of the flight path angle suggests that the feedback controller is partially effective in compensating for disturbances,

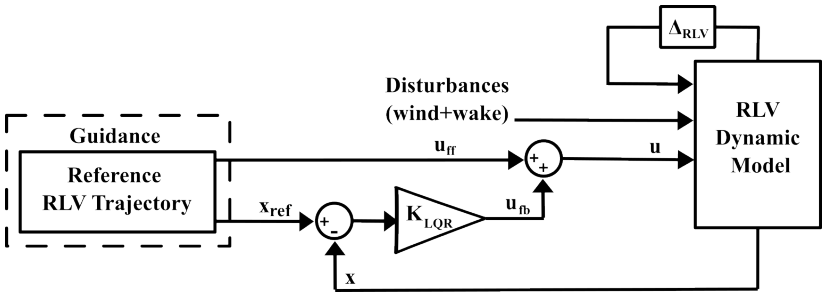

Figure 11: Closed-loop system architecture for the RLV

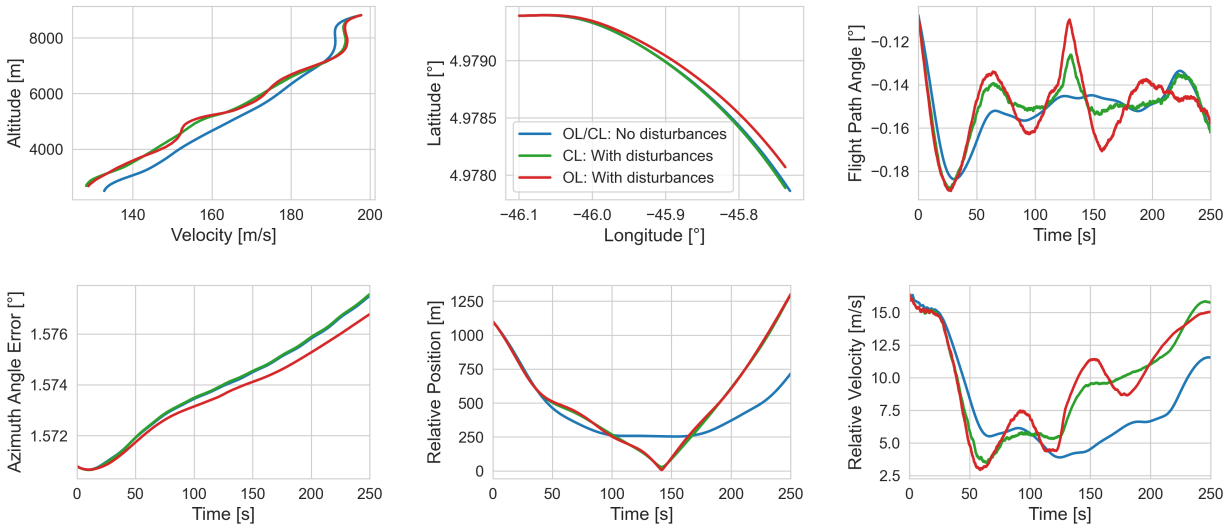

Figure 12: Trajectory simulations of the RLV - Open loop and closed loop performance

DOI: 10.13009/EUCASS2025-527

though not entirely. The latitude-longitude trajectory of the closed-loop case shows better alignment with the nominal path compared to the open-loop case. Additionally, the relative velocity with respect to the target vehicle exhibits pronounced oscillations in the open-loop scenario, whereas the closed-loop response is noticeably more stable. These observations indicate that the feedback controller is contributing to disturbance rejection, but to a limited extent. A more detailed analysis of the individual disturbance effects is carried out in the following section to better understand the root causes and propose possible improvements to the controller.

4.1 Effect of disturbances

As described in Section 2.3, three environmental uncertainties or external disturbances are considered in this study: atmospheric density variation, TA wake, and wind. To isolate their individual effects, closed-loop trajectory simulations are conducted by applying each disturbance independently, while assuming a nominal initial state. Figure 13 shows the impact of each disturbance (deviation from nominal) on the RLV trajectory. The relative position and velocity with respect to the TA is also shown to analyse the affect on reaching the mating zone. As shown in the figure, atmospheric density variation has the least impact on the trajectory, followed by the TA wake, which introduces small but noticeable deviations. Wind, however, causes the most significant deviation from the nominal path.

The effect of atmospheric density appears throughout the trajectory but remains small and resembles high-frequency noise. The controller is able to track the reference effectively in this case, with no substantial loss in the time spent by the RLV in the mating zone. This is confirmed by Table 2, which shows the time spent in the mating zone for each disturbance scenario, compared to the nominal trajectory without disturbances. Furthermore, the open-loop performance is also marginally affected by this disturbance.

Table 2: Effect of disturbances on time spent in mating zone

Mode	**No disturbance**	**Atmospheric density**	**Aircraft Wake**	**Wind**
OL Time [s]	21.4	20.4	18.3	0
CL Time [s]	21.4	20.8	21.1	0

From Figure 13, it can be observed that the effects of the aircraft wake are noticeable only during a brief period between 100 and 170 s, when the RLV is behind the TA and in close proximity. From the figure, errors as large as 17 m in altitude, 1 m/s in velocity, and 0.5° in flight path angle can be observed due to the wake disturbance. Nevertheless, the RLV is able to correct for these deviations using the feedback controller. As indicated by the time spent in the mating zone (see table 2), the closed-loop system outperforms the open-loop in mitigating these errors. There is no significant reduction in mating zone time, primarily because the RLV is only briefly exposed to the wake and passes through it quickly.

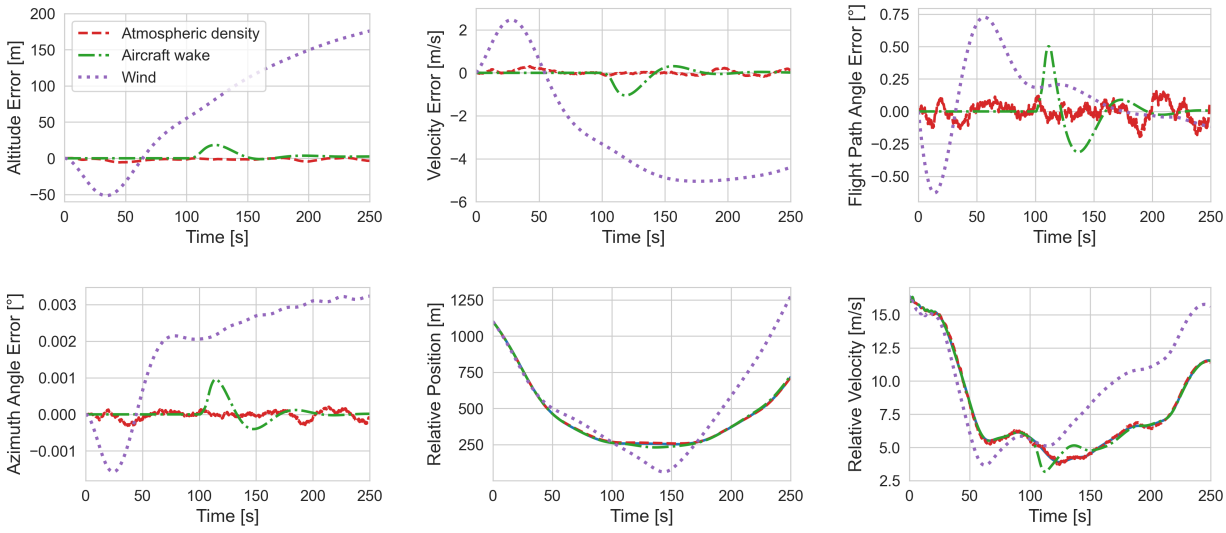

Figure 13: Trajectory simulations of the RLV - Effect of disturbances when applied individually on nominal trajectory

DOI: 10.13009/EUCASS2025-527

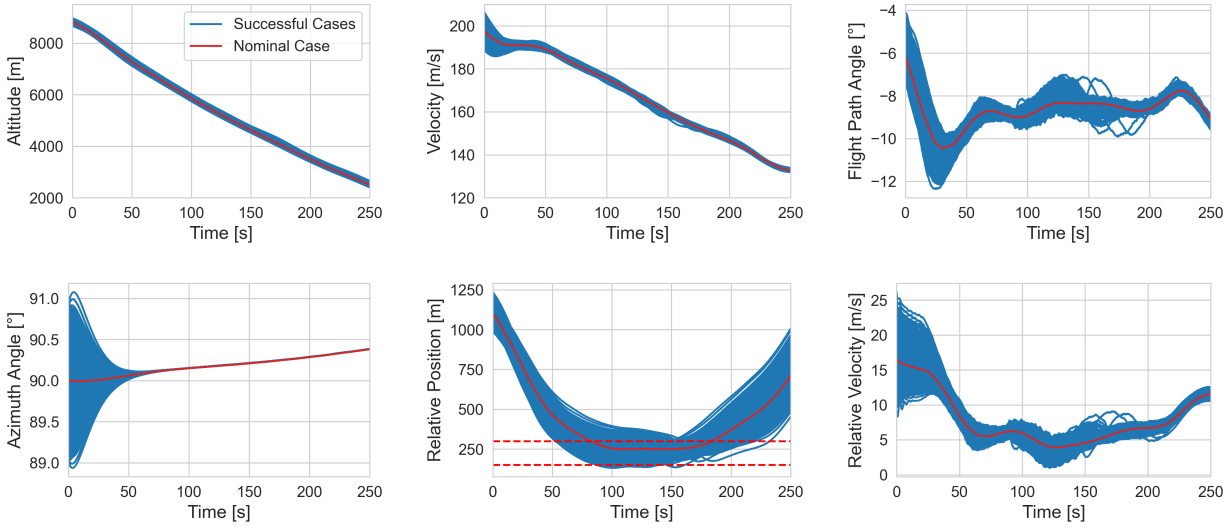

Figure 14: Trajectory simulations of the RLV - Monte Carlo Distribution

Wind has the most significant impact among the considered disturbances and cannot be effectively compensated by the feedback controller. As shown in Figure 4, the zonal wind component varies continuously between -8 m/s and 2 m/s. This variation alters the aerodynamic coefficients of the RLV, resulting in substantial deviations in velocity and, consequently, altitude. Figure 13 shows that altitude error drifts to nearly 200 m, and the velocity error closely follows the trend of the wind profile. As a result, the RLV fails to enter the mating zone, making capture unfeasible. Table 2 confirms that this outcome holds for both the open-loop (OL) and closed-loop (CL) scenarios.

These results highlight the need for further controller development to effectively compensate for wind disturbances. Given that the IAC procedure demands high-precision maneuvering for successful capture, it is critical to mitigate the effects of wind. One potential approach is to integrate a wind observer into the controller, as proposed by Simplicio et. al.[24] This observer will be incorporated in future studies to enhance robustness against wind-induced errors. In the current study, and in the Monte Carlo (MC) simulations presented in the following section, the wind disturbance is excluded under the assumption that it can be corrected, in order to analyse the performance limits of the guidance and control system.

4.2 Monte Carlo simulations

In this study, a MC analysis is performed to establish feasibility boundaries and re-planning criteria for the proposed guidance trajectory and control scheme. By evaluating performance under realistic variations in initial conditions and environmental disturbances, the study enables a statistical assessment of robustness outside the nominal scenario. Table 3 presents the range of initial state dispersions used in the study, defined as the 3σ bounds of a normal distribution. The position errors are introduced in the NED (North-East-Down) coordinate frame for easier interpretation and clearer physical understanding of the deviations from the nominal initial state. In addition to these variations, the effects of aircraft wake and uncertainty in atmospheric density are also considered. A MC trajectory is considered feasible if it arrives within the bounds of the mating zone. It is assumed that the tether length can vary between 150 m and 300 m using a winch mechanism, and any trajectory that reaches this relative position with a relative velocity less than 10 m/s behind the aircraft is considered feasible for capture.

Figure 14 shows the MC distribution of 1000 CL successful trajectories in comparison to the nominal trajectory (without disturbances). Minor deviations can be seen in the flight path angle profiles due to brief exposure to aircraft wake. While the guidance and control system enabled many successful outcomes, the overall CL success rate was 46.2% within the initial error bounds defined in Table 3. Although this represents an improvement over the OL trajectories, which achieved only a 8.8% success rate, further investigation is required to identify the feasible conditions that yield a consistently high success rate.

Figure 15 shows the Monte Carlo distribution of successful cases plotted against initial altitude and initial velocity. The color of each scatter point represents the time spent in the mating zone. Trajectories that spend 20 s or more in the mating zone are assumed to allow for multiple capture attempts by the capturing device, while shorter durations

DOI: 10.13009/EUCASS2025-527

Table 3: Common 3σ dispersion in different initial states for MC analysis

State	MC
Distance North [m]	±150
Distance East [m]	±150
Distance Down [m]	±150
Velocity Modulus [m/s]	±20
Azimuth Angle [°]	±1
Flight Path Angle [°]	±1
Angle of Attack [°]	±2
Bank Angle [°]	±2

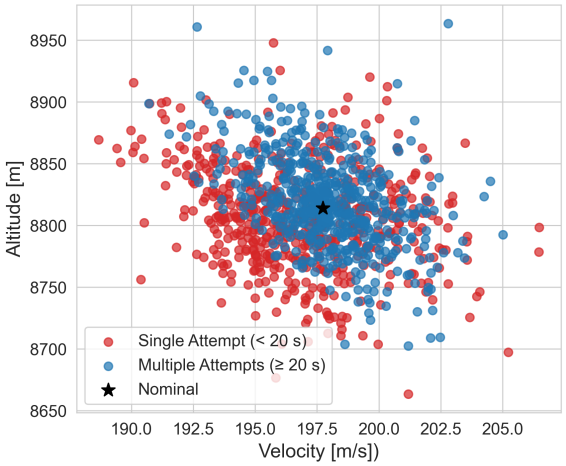

Figure 15: Monte Carlo Distribution: Effect of initial velocity and altitude on mating time

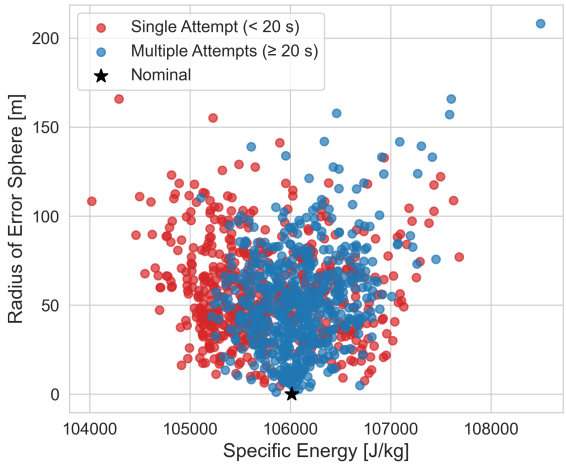

Figure 16: Monte Carlo Distribution: Effect of position error and energy on mating time

correspond to only a single attempt. From the figure, it can be observed that most successful trajectories that allow for multiple capture attempts tend to start closer to the nominal initial conditions than those allowing only a single attempt. Additionally, there appears to be a trade-off between altitude and velocity deviations - positive deviations in altitude require lower initial velocities, while negative deviations require higher velocities. This aligns with expectations, as the unpowered RLV must possess an appropriate amount of energy to successfully follow the guidance trajectory. If the total energy is either too high or too low, the guidance becomes infeasible.

Table 4: Dispersion distribution by radius for 1000 successful cases

Radius [m]	0–50	50–100	100–150	>150
Single Attempt	227	173	51	2
Multiple Attempts	265	251	27	4
Total (CL)	492	424	78	6

Figure 16 shows the Monte Carlo dispersion over the radius of the error sphere, plotted against the specific energy (energy per unit mass). The error sphere represents the magnitude of the initial position error in 3D space, combining deviations in the north, east, and down directions. It is defined as:

$$r = \sqrt{\Delta x_{north}{}^2 + \Delta y_{east}^2 + \Delta z_{down}^2}$$

where r gives the scalar distance from the nominal initial position. The scattered points in Figure 16 represent successful closed-loop trajectories, color-coded based on the time spent in the mating zone. The figure shows that trajectories resulting in multiple capture opportunities tend to cluster near the nominal point, both in terms of energy and positional accuracy. In contrast, single-attempt cases are more dispersed, often lying at the edges of the feasible region. This indicates that maintaining initial conditions within a bounded region around the nominal state in both energy and spa-

DOI: 10.13009/EUCASS2025-527

tial error could improve the chances of successful capture. Table 4 further quantifies the relationship between the time spent in the mating zone and the magnitude of the initial spatial error at the start of the maneuver.

Based on Figure 16 and Table 4, feasibility can be significantly improved by constraining the initial error sphere radius to within 100 m and the error in specific energy to within ±1.5% of the nominal value. When the MC simulations were repeated under these constraints, the closed-loop success rate increased to 88.7%. This result provides a basis for defining a trajectory replanning criterion - if the initial spatial and energy errors exceed the specified bounds, a new guidance trajectory must be computed to ensure successful rendezvous.

5. Conclusion

This study focuses on the guidance and control performance of a reusable launch vehicle (RLV) during the rendezvous maneuver in the In-Air Capturing (IAC) recovery method. IAC is a novel recovery concept in which RLV stages are retrieved mid-air using a towing aircraft (TA). During this, the RLV executes an unpowered glide to reach a designated position - known as the mating zone - behind the TA, where it is captured by an autonomous, tethered device. A typical control strategy is employed, where a precomputed nominal trajectory serves as guidance, and the controller compensates for deviations from the expected state. While the optimised guidance path was developed in prior work, this study introduces and integrates a gain-scheduled Linear Quadratic Regulator (LQR) as a robust control solution to enable accurate tracking during the critical gliding formation and capture phase.

The proposed controller adapts its gains based on the energy state of the RLV, allowing for reliable performance across a wide range of operating conditions. The complete system was evaluated through closed-loop trajectory simulations, considering multiple external disturbances and initial condition offsets. A detailed Monte Carlo campaign was conducted to assess robustness and quantify the time spent in the mating zone, which serves as a key indicator of capture feasibility.

The study demonstrated that the controller performed well under disturbances such as atmospheric density variations and wake effects but was unable to compensate for wind. In the presence of wind, the RLV failed to reach the mating zone, resulting in an unsuccessful capture. To address this limitation, the inclusion of a wind observation model is proposed for future iterations of the control system. As a result, the Monte Carlo study is performed without wind disturbances, under the assumption that wind effects can be corrected for.

Additionally, results from Monte Carlo simulations showed that capture feasibility can be significantly improved by constraining the initial error sphere radius to within 100 m and the specific energy error to within ±1.5% of the nominal value. When the simulations were repeated under these conditions, the closed-loop success rate increased from 46.2% to 88.7%. This finding provides a basis for defining a trajectory re-planning criterion: if the initial spatial and energy errors exceed the specified bounds, a new guidance trajectory must be computed to ensure successful rendezvous.

6. Acknowledgments

The author acknowledges the use of AI-based language tools to support the editing and refinement of the manuscript.

References

[1] A. Marwege, A. Gülhan, J. Klevanski, et al. RETALT: review of technologies and overview of design changes. *CEAS Space Journal*, 14:433–445, 2022.

[2] M. Sippel, S. Singh, and S. Stappert. RLV-return mode “In-Air-Capturing” and definition of its development roadmap. In *9th European Conference on Aeronautics and Space Sciences (EUCASS)*, 2022.

[3] I. Dietlein, L. Bussler, S. Stappert, J. Wilken, and M. Sippel. Overview of system study on recovery methods for reusable first stages of future european launchers. *CEAS Space Journal*, pages 1–18, 2024.

[4] J. Wilken, M. Herberhold, and M. Sippel. Options for future european reusable booster stages: evaluation and comparison of VTHL and VTVL costs. *CEAS Space Journal*, 17(1):177–198, 2025.

[5] S. Singh, M. Sippel, and S. Stappert. Full-scale simulations of ‘In-Air Capturing’ return mode for winged reusable launch vehicles. *Journal of Physics: Conference Series*, 2526(1):012114, 2023.

[6] S. Singh, S. Stappert, L. Bussler, M. Sippel, Y. C. Kucukosman, and S. Buckingham. Full-scale simulation and analysis of formation flight during in-air capturing of a winged reusable launch vehicle. *Journal of Space Safety Engineering*, 9(4):541–552, 2022.

DOI: 10.13009/EUCASS2025-527

[7] P. R. Thomas, U. Bhandari, S. Bullock, T. S. Richardson, and J. L. Du Bois. Advances in air-to-air refuelling. *Progress in Aerospace Sciences*, 71:1–35, 2014.

[8] S. Singh, S. Stappert, S. Buckingham, S. Lopes, Y. C. Kucukosman, M. Simioana, and P. Planquart. Dynamic modelling and control of an aerodynamically controlled capturing device for 'In-Air-Capturing' of a reusable launch vehicle. In *11th International ESA Conference on Guidance, Navigation and Control Systems*, 2021.

[9] S. Singh, M. Simioana, S. Stappert, M. Sippel, S. Buckingham, S. Lopes, and Y. C. Kucukosman. Control design and analysis of a capturing device performing In-Air Capturing of a reusable launch vehicle. In *9th European Conference on Aeronautics and Space Sciences (EUCASS)*, 2022.

[10] S. Singh and M. Mastrogiuseppe. Multibody modelling of tether and capture system for dynamic simulations of in-air capturing. *Acta Astronautica*, 218:59–69, 2024.

[11] S. Singh, L. Bussler, S. Stappert, M. Sippel, Y. C. Kucukosman, and S. Buckingham. Simulation and analysis of pull-up manoeuvre during in-air capturing of a reusable launch vehicle. In *9th European Conference for Aeronautics and Space Sciences (EUCASS)*, 2022.

[12] S. Singh and M. Sagliano. Optimal control-based design and feasibility assessment of rendezvous trajectories for in-air capturing of a reusable launcher stage, 2025. Under review at Acta Astronautica.

[13] M. Sippel, S. Stappert, L. Bussler, and C. Messe. Powerful and flexible future launchers in 2- or 3-stage configuration. In *Proceedings of 70th International Astronautical Congress*, 2019.

[14] G. Norris and M Wagner. Airbus a340 and a330 (jetliner history), 2001.

[15] Y. C. Kucukosman, S. Lopes, S. Buckingham, P. Planquart, S. Singh, L. Bussler, S. Stappert, and M. Sippel. Aerodynamic characterization of in-air capturing vehicles using cfd simulations. In *9th European Conference on Aeronautics and Space Sciences (EUCASS)*, 2022.

[16] S. Stappert, S. Singh, and M. Sippel. Developing an innovative and high-performance method for recovering reusable launcher stages: The in-air-capturing method. *CEAS Space Journal*, 2023.

[17] N. X. Vinh. Optimal trajectories in atmospheric flight. *Space mankind's fourth environment*, pages 449–468, 1982.

[18] D. P. Drob, J. T. Emmert, G. Crowley, J. Picone, G. Shepherd, W. Skinner, P. Hays, R. J. Niciejewski, M. Larsen, C. Y. She, et al. An empirical model of the earth's horizontal wind fields: HWM07. *Journal of Geophysical Research: Space Physics*, 113(A12), 2008.

[19] P. H. Zipfel. *Modeling and simulation of aerospace vehicle dynamics*. AIAA, 2000.

[20] S. B. Pope. *Turbulent Flows*. Cambridge University Press, 2000.

[21] M. A. Patterson and A. V. Rao. GPOPS-II: A MATLAB software for solving multiple-phase optimal control problems using hp-adaptive gaussian quadrature collocation methods and sparse nonlinear programming. *ACM Transactions on Mathematical Software (TOMS)*, 41(1):1–37, 2014.

[22] H. Lee. *Linearization of nonlinear control systems*. Springer, 2022.

[23] K. Ogata. *Modern control engineering*. Prentice Hall, 2009.

[24] P. Simplício, A. Marcos, and S. Bennani. Launcher flight control design using robust wind disturbance observation. *Acta Astronautica*, 186:303–318, 2021.